Article

Effects of High Magnetic Fields on Phase Transformations in Amorphous $Nd_2Fe_{14}B$

Michael S. Kesler [1], **Brandt A. Jensen** [2], **Lin Zhou** [2], **Olena Palasyuk** [2], **Tae-Hoon Kim** [2], **Matthew J. Kramer** [2], **Ikenna C. Nlebedim** [2], **Orlando Rios** [1] **and Michael A. McGuire** [1,*]

[1] Oak Ridge National Laboratory, 1 Bethel Valley Road, Oak Ridge, TN 37831, USA; keslerms@ornl.gov (M.S.K.); rioso@ornl.gov (O.R.)

[2] Ames Laboratory, 311 Iowa State University, Ames, IA 50011, USA; brandtj@ameslab.gov (B.J.); linzhou@ameslab.gov (L.Z.); opalasy@ameslab.gov (O.P.); thkim@ameslab.gov (T.-H.K.); mjkramer@ameslab.gov (M.J.K.); nlebedim@iastate.edu (I.C.N.)

* Correspondence: mcguirema@ornl.gov; Tel.: +1-865-574-5496

check for updates

Abstract: We briefly summarize the results from a set of experiments designed to demonstrate the effects of high magnetic fields applied during thermal annealing of amorphous $Nd_2Fe_{14}B$ produced through melt-spinning. A custom-built differential scanning calorimeter was used to determine the crystallization temperatures in zero-field and in applied fields of 20 kOe and 90 kOe, which guided subsequent heat treatments to evaluate phase evolution. X-ray diffraction was used for phase identification and transmission electron microscopy was employed for observation of the crystallite size and morphology. Magnetization measurements were also used to evaluate the resulting magnetic phases after thermomagnetic processing. While the applied magnetic fields do not appear to affect the crystallization temperature, significant effects on the kinetics of phase evolution are observed and correlated strongly to the magnetic behavior.

Keywords: thermomagnetic processing; permanent magnet materials; $Nd_2Fe_{14}B$; X-ray diffraction; magnetometry

1. Introduction

Nd-Fe-B permanent magnets offer a high energy product for near-ambient temperature sintered and bonded magnet applications [1–3]. In this and all permanent magnet materials, the magnetic performance is tied closely to the microstructure. Processing protocols are designed to optimize remanence and coercivity through controlling crystallite sizes and crystallographic texture, as well as chemistry and grain boundary properties. The promise and potential associated with advanced microstructural control is highlighted by recent demonstrations that grain size reduction [4,5] and careful control of grain boundary thickness and composition [6] can enable coercivities previously only achieved through the addition of the scarce and high-cost element dysprosium. Thus, novel approaches to magnet processing warrant exploration in the pursuit of developing optimized microstructures for improved magnetic performance.

High magnetic fields applied during heat treatments (thermomagnetic processing) can be used to tune microstructures by affecting both thermodynamic phase equilibria [7,8] and kinetic behavior [9,10], in particular in magnetic materials [11]. Several opportunities for manipulation are evident in thermomagnetic processing, including crystallographic texturing, and preferential phase morphology. Some less intuitive effects are microstructural refinement, stabilization of phase fields to higher and/or lower temperatures, and hastening or slowing of kinetics. Several thermomagnetic processing studies on systems targeting the 2:14:1 hard magnetic phase are found in literature [11–16].

In the Nd-Co-B system [15], improvements in coercivity were attributed to the field-induced increase in volume fraction of the ferromagnetic $Nd_2Co_{14}B$ phase due to the higher relative moment compared to the paramagnetic amorphous ribbon precursor. The ferromagnetic Nd_2Co_{17} phase and α-Co were also promoted and dominated above the Curie temperature of $Nd_2Co_{14}B$ resulting in lower coercivity compared to the zero-field annealing. In the Pr-Co-B system [16] the magnetic field exhibited a deleterious effect on coercivity due to the stabilization of the Pr_2Co_{17} phase to higher annealing temperatures, though significant microstructural refinement was observed. Both of these Co-containing systems have a high moment, high Curie temperature phase (2:17) that appears to affect the phase evolution at high fields. The Nd-Fe-B system presents a contrasting comparison due to the absence of the 2:17 phase in the relevant alloy composition space, along with the low Curie temperature of the $Nd_2Fe_{14}B$ phase.

The current work explores the effect of high field thermomagnetic processing on the microstructural evolution and magnetic behavior of $Nd_2Fe_{14}B$ ribbons produced through melt-spinning with TiC additions. A custom-built differential scanning calorimeter (DSC) was used to determine the crystallization temperatures at zero-field and applied fields of 20 kOe and 90 kOe, which guided subsequent heat treatments to evaluate phase evolution. X-ray diffraction (XRD) was used for phase identification and transmission electron microscopy (TEM) was employed for observation of the microstructural size, morphology, and magnetic domain structure. A superconducting quantum interference device (SQUID) and vibrating sample magnetometer (VSM) were used to measure the magnetic behavior. The high magnetic fields do not appear to affect crystallization temperatures; however, kinetics, and perhaps phase stability, are significantly altered during phase evolution, and this is reflected strongly in the microstructural and magnetic properties.

2. Results

Melt-spinning is a common method for processing fine microstructures in magnetic materials for use in bonded and sintered magnet applications. Introducing Ti and C to Nd-Fe-B for the melt-spinning process has been shown to improve the glassy formability thus enabling production of fully amorphous ribbons [17]. The addition of 3 wt.% TiC to the stoichiometric $Nd_2Fe_{14}B$ inhibited nucleation of phases during the melt spinning process, and an optical micrograph of the ribbons is shown in Figure 1a. Upon heating, amorphous $Nd_2Fe_{14}B$ + TiC is known to undergo crystallization at about 625 °C [17]. To examine the effect of magnetic field on the crystallization temperature, we employed a custom-built calorimeter designed for operation in high magnetic fields [18]. Figure 1b shows DSC curves of the as-spun ribbons as they were heated through the crystallization temperature at zero-field and applied fields of 20 kOe and 90 kOe. The onset temperatures from crystallization in the DSC were measured by the tangent method and are listed in Table 1. Little variation was observed in the position or shape of the exothermic peaks signifying crystallization; however, effects on more subtle aspects of the kinetics may be expected. Thus, heat treatments were designed to evaluate the phase evolution during annealing near the crystallization temperature. Heat treatment temperatures are indicated by the vertical dashed lines in Figure 1b, and were chosen to be below, near, and above the crystallization peak observed in the DSC.

Table 1. Crystallization onset temperatures measured from DSC data shown in Figure 1b.

Applied Field (kOe)	Onset Temperature (°C)
0	624
	624
20	625
	622
90	624
	626
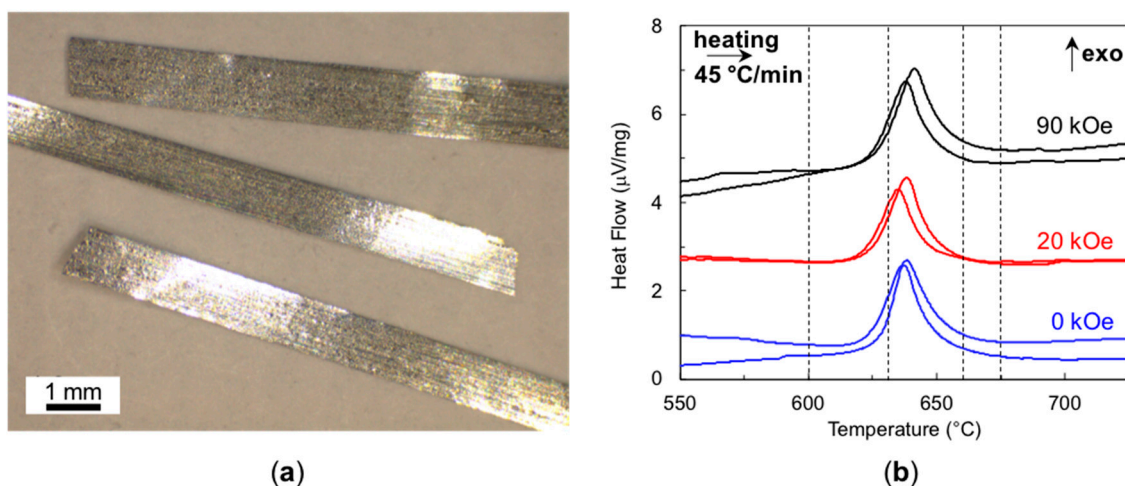
Figure 1. (**a**) Optical micrograph of the 'wheel side' of the $Nd_2Fe_{14}B$ + TiC melt-spun ribbons and (**b**) DSC curves showing the exothermic peak during crystallization of the $Nd_2Fe_{14}B$ as-spun ribbons at zero-field (blue) and applied fields of 20 kOe (red) and 90 kOe (black). Data are shown for two different samples for each field. Dashed vertical lines indicate the temperatures chosen for the heat treatments.

As-spun ribbons were evaluated with XRD (gray curve in Figure 2a) revealing a pattern characteristic of an amorphous material. The data were collected from the surface of the ribbon on the 'free side', which is the side that was not in contact with the copper wheel during melt-spinning. The 'free side' of the ribbon cooled more slowly, so if crystallization were to occur, it would be most evident in XRD from this surface [19].

The melt-spun samples were heat treated at annealing temperatures of 600 °C and 660 °C for 30 min at zero-field and applied fields of 20 kOe and 90 kOe, and the results are shown in Figure 2. Heating for 30 min at 600 °C, slightly below the crystallization temperature indicated during dynamic heating in DSC, yielded significantly different results depending on the applied field. The XRD spectra shown in Figure 2a revealed an apparent amorphous signal at zero-field (blue curve), significant crystallization of the $Nd_2Fe_{14}B$ phase at 20 kOe (red curve), and an apparent amorphous signal with a clear α-Fe (110) peak at 90 kOe.

To complement the XRD results, magnetometry was conducted (shown in Figure 2b) on the as-spun and annealed ribbons. The magnetic behaviors are seen to be generally consistent with the XRD results. At 20 kOe, the crystallization of $Nd_2Fe_{14}B$ results in hard magnetic behavior, while at 90 kOe, the presence of α-Fe and an otherwise amorphous material has a higher magnetic moment but has entirely soft magnetic behavior. The as-spun and zero-field annealed samples show mostly soft magnetic behavior, but the deviation from soft behavior of the gray and blue curves in the third quadrant in Figure 2b indicates that some phase fraction of a hard phase has precipitated and slightly more so in the zero-field annealed sample. It is likely that the $Nd_2Fe_{14}B$ phase has formed a relatively small phase fraction of ultrafine precipitates in these two samples that are below the detection limit of XRD.

The observation of very soft magnetic behavior and only Fe in XRD for the sample heated at 600 °C (below the crystallization temperature) in a 90 kOe field is quite striking and indicates a strong preference for formation/growth of Fe over $Nd_2Fe_{14}B$ under these conditions. Although a more detailed study would be required to fully understand this interesting observation, we can speculate that this may arise due to simultaneous thermodynamic and kinetic effects associated with the field and temperature. The thermodynamic stabilization of high moment phases by large magnetic fields has been previously reported in the literature [16] and theoretically predicted based on the free energy of formation calculations [7]. The annealing temperature of 600 °C is well above the Curie temperature of $Nd_2Fe_{14}B$ (~320 °C) and below that of Fe (770 °C), which would be consistent with the promotion of Fe formation. The observation of slight magnetic behavior in the as-spun material, followed by

the entirely soft behavior and the α-Fe peak in XRD after annealing at 90 kOe (Figure 2a,b) suggests that the Fe phase is supplanting the $Nd_2Fe_{14}B$ nuclei present in the as-spun material. At 600 °C, the diffusion of Nd is expected to be rather sluggish compared to Fe. This could explain the formation of Fe, wherein the Fe-rich embryos of Nd2Fe14B transform into stabilized α-Fe resulting in Nd-rich (or Fe denuded) zones around the α-Fe, thus limiting further growth. Annealing at 600 °C and an applied field of 20 kOe appears to encourage the precipitation and growth of $Nd_2Fe_{14}B$ perhaps due to weaker magnetic stabilization of the α-Fe in this lower field, thus limiting the denuded zone. The existing Fe phase can provide nucleation sites for the $Nd_2Fe_{14}B$ phase and, once formed, they have enough thermal energy to grow into the near-stoichiometric composition of the amorphous matrix. We note that other thermodynamic or kinetic effects must also be at play, since this scenario alone cannot explain the observed results for the ribbons heated in zero-field, which showed little growth of $Nd_2Fe_{14}B$ in magnetic or diffraction data.
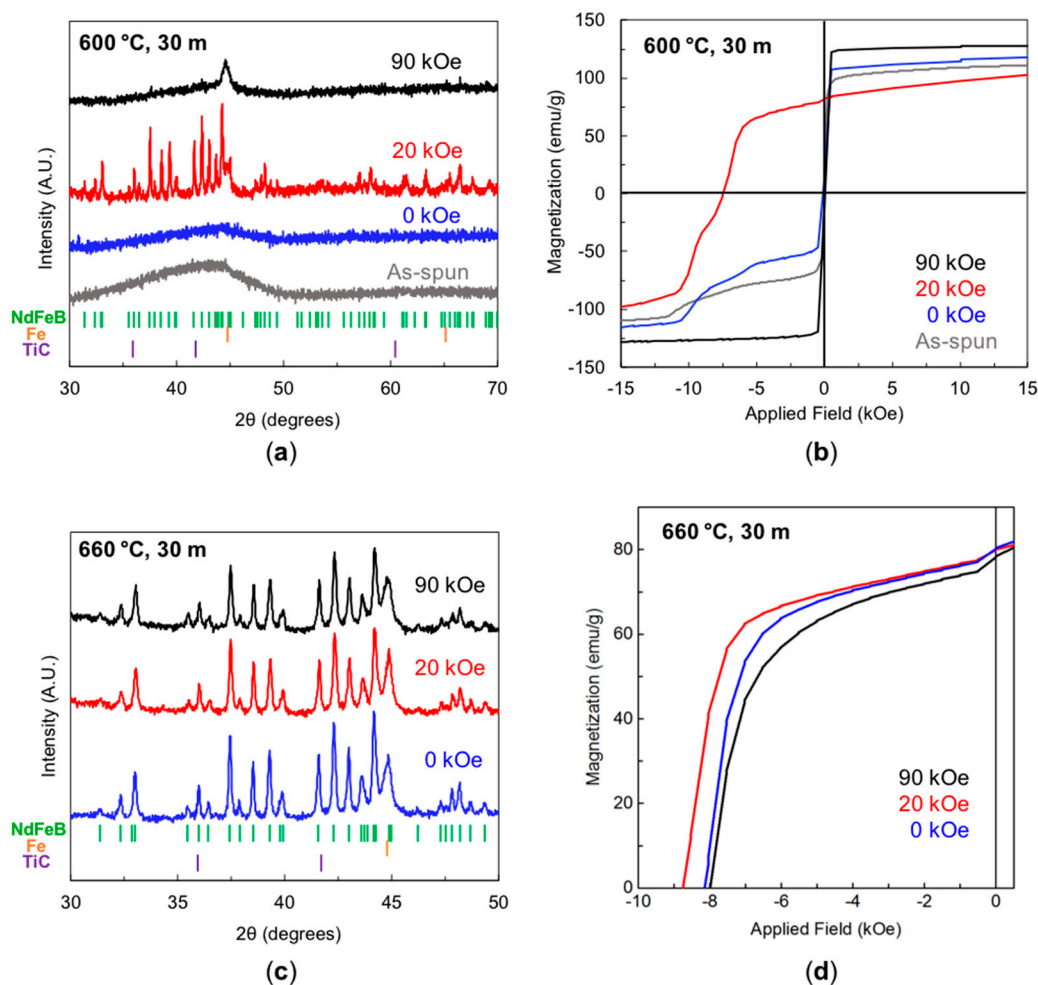
Figure 2. Characterization of $Nd_2Fe_{14}B$ ribbons after annealing for 30 min at 600 °C showing (**a**) XRD (Cu Kα1 radiation, λ = 1.5406 Å) spectra and (**b**) isothermal magnetization curves (SQUID) measured at room temperature upon decreasing the field, and after annealing for 30 min at 660 °C showing (**c**) XRD and (**d**) isothermal magnetization curves.

Annealing at a higher temperature of 660 °C (above the crystallization temperature) for 30 min resulted in the formation of $Nd_2Fe_{14}B$ (Figure 2c) and in hard magnetic properties independent of the applied field (Figure 2d). All specimens show a slight soft component in the M-H plot (a kink near zero applied field) likely indicating the presence of Fe. This soft component appears to be larger in the sample annealed at 90 kOe, like the behavior described above for the lower heat treatment

temperature (600 °C). At 660 °C, diffusion of Nd occurs more readily in all cases such that $Nd_2Fe_{14}B$ forms more easily, and the α-Fe moment is beginning to be suppressed as the Curie temperature is approached [20,21], limiting the magnetic field's effect on phase equilibrium at this temperature. Comparison of the demagnetization curves shows that the 20 kOe field case has the highest coercivity and an equivalent remanent magnetization to the zero-field case, while the 90 kOe case showed a slight suppression of both properties. It is interesting to note that at the two temperatures examined here, both above and below the crystallization temperature, intermediate magnetic fields (20 kOe) produced the best magnetic performance in terms of moment and coercivity.

To further explore the phase evolution, ribbons were annealed at shorter times, 3 min and water quenched, to interrupt the microstructural evolution prior to achieving a state of equilibrium. It should be noted here that, due to the experimental setup described in the Materials and Methods, there was certainly a temperature lag between the thermocouple that lay outside of the sealed quartz ampule and the Ta foil-wrapped specimen such that the temperature reported was not the exact temperature of the specimen during this short heating time. Figure 3a,b display bright field TEM micrographs and selected area diffraction (SAD) patterns for zero-field and 90 kOe annealing, respectively. At 630 °C, the zero-field case resulted in significant precipitation of $Nd_2Fe_{14}B$ particles, while at 90 kOe, no precipitation is observed in TEM after the same annealing treatment. The SAD patterns, inset in Figure 3a,b, are consistent with the observations from the TEM micrographs as the zero-field case shows more discreet ring formation compared to the haloed ring pattern in the inset of Figure 3b. However, the magnetic behavior, shown in Figure 3c,d, suggests that in both cases some hard component is present, with a greater phase fraction in the zero-field case. The evidence of hard phase formation at 630 °C in the magnetization measurement from the 90 kOe annealed ribbon without corroborating evidence from TEM is owed to the bulk and selective sampling of the two techniques, respectively. Further investigation in TEM could reveal extremely fine particles in the 90 kOe annealed ribbons.

A similar trend in magnetic behavior with the processing field is observed after heating for 3 min at lower temperature (600 °C) and higher temperature (660 °C): heating in the 90 kOe field suppresses the development of the hard magnetic phase (Figure 3c,d). The results from the 3 min anneals allude to a kinetic effect where the high magnetic field is slowing the growth of precipitates.

Similar to the results of the 30 min anneals, at 600 °C the high field appears to favor the softer phase with a high moment, α-Fe, but the short anneal does not allow time for the transformation from the existing hard phase to the α-Fe to fully occur. Additionally, at higher temperatures, the Nd-rich region formed around the Fe nuclei upon heating acts as a kinetic barrier slowing the nucleation of the hard phase when comparing to the zero-field case. While a clear understanding of these effects of would require a more detailed study, a possible explanation for the observations could be posed as follows. The field-induced suppression of the precipitation of the hard phase may be due to the initial precipitation of α-Fe and dissolution of $Nd_2Fe_{14}B$ upon heating. An Fe-denuded zone forms, limiting the ability for the $Nd_2Fe_{14}B$ phase to readily nucleate or grown. Once enough thermal energy is present, Nd atoms can diffuse from the denuded zone into Fe-rich regions and the local composition becomes favorable again for the formation of $Nd_2Fe_{14}B$. While these processes occur on short time and length scales, it is enough to affect the growth of the hard phase. In contrast, in the zero-field case, there is no increased driving force for the formation of Fe and the dissolution of the nucleated hard phase upon heating.

In the final experiment presented here, an annealing temperature of 675 °C was selected to ensure full crystallization and a time of 15 min was used to limit the coarsening of the microstructures. The results from these experiments are shown in Figure 4. TEM micrographs display the resulting crystallized microstructure revealing an apparent slight increase in grain size for the zero-field case (Figure 4a), compared with the 90 kOe case (Figure 4b) and SAD pattern insets support this, wherein the polycrystalline spots in Figure 4b are closer to forming discreet rings suggesting a larger sampling of grains. The XRD spectra for 675 °C annealed ribbons (Figure 4c) are nearly identical with no

indication of differences in α-Fe formation. The VSM results in Figure 4d show two closely overlaid magnetic hysteresis curves for the two samples annealed at 675 °C. The remanent magnetizations (81 emu/g) and maximum energy products (12 MGOe) are the same for the samples annealed in zero and 90 kOe fields; however, the coercivity of the sample annealed at 90 kOe is slightly higher than that of the sample annealed in zero-field (9.7 vs. 9.4 kOe, respectively). Considering the only observed deviation in magnetic properties is this increased coercivity, a slight reduction in grain size from the 90 kOe annealing is the likely cause. Individual pseudo-Voigt profiles were fit to eight single indexed diffraction peaks in the 2θ range of 41–51 degrees from the diffraction patterns shown in Figure 4c. For each of these reflections the breadth of the fitted peak was larger by 3–7% in the sample processed at 90 kOe compared to the sample processed in zero-field. This is consistent with a slightly smaller particle size in the 90 kOe sample. Assuming the peak broadening is all due to crystallite size effects, and a Sherrer constant of 1, approximate particle size is estimated to be 40 nm, consistent with the microscopy shown in Figure 4a,b. On heating in the 90 kOe field, initially the formation of Fe is promoted, but this is only a transient effect. Upon reaching the temperature range that the nucleation of $Nd_2Fe_{14}B$ is favored, the Fe nuclei must be dissolved, delaying the nucleation and growth of the $Nd_2Fe_{14}B$, hence slightly reducing their grain size compared to the zero-field case.
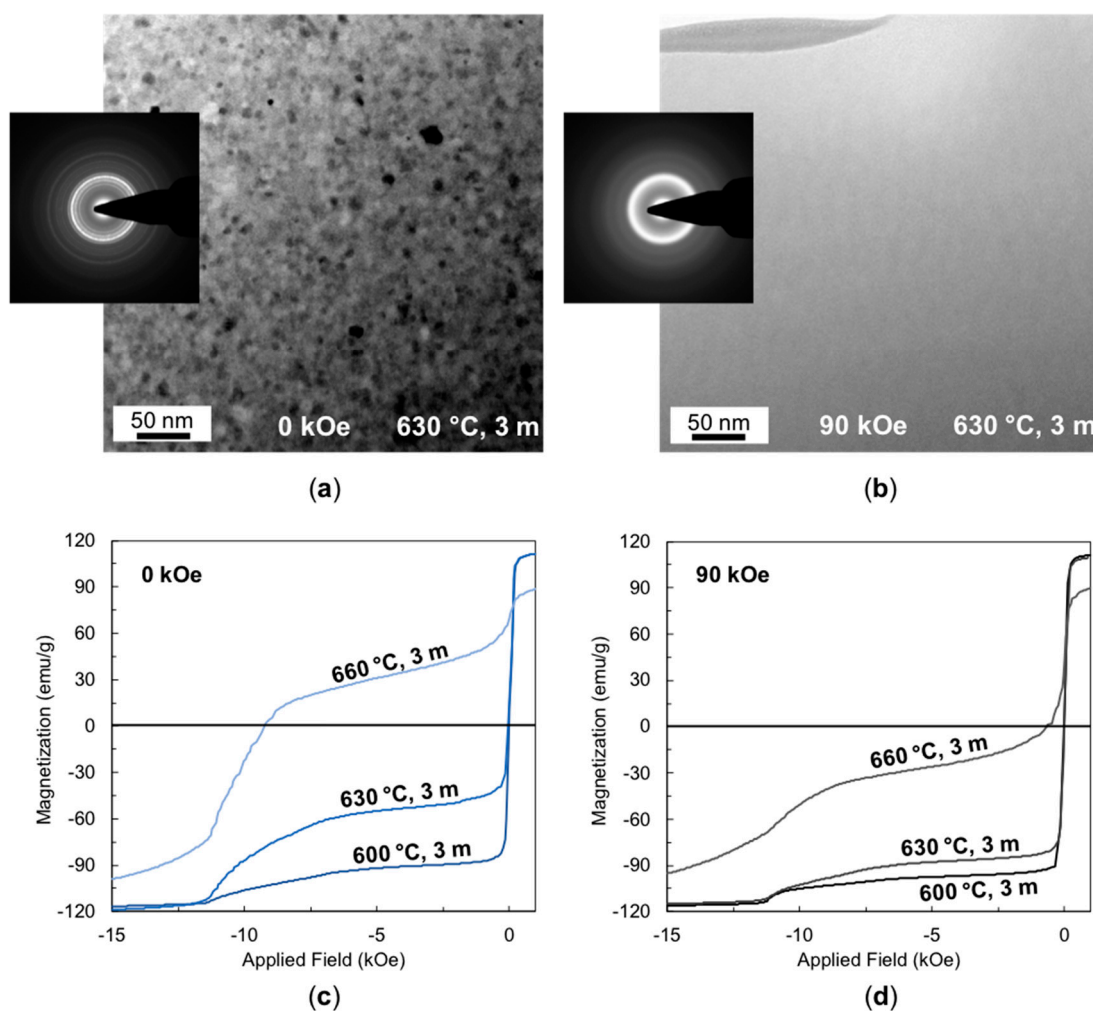
Figure 3. TEM bright field micrographs with SAD pattern insets from $Nd_2Fe_{14}B$ ribbons annealed at 630 °C for 3 min at (**a**) zero-field and (**b**) in an applied field of 90 kOe. VSM demagnetization curves from samples annealed at (**c**) zero-field and (**d**) in an applied field of 90 kOe showing the magnetic behavior evolution with increasing annealing temperature.
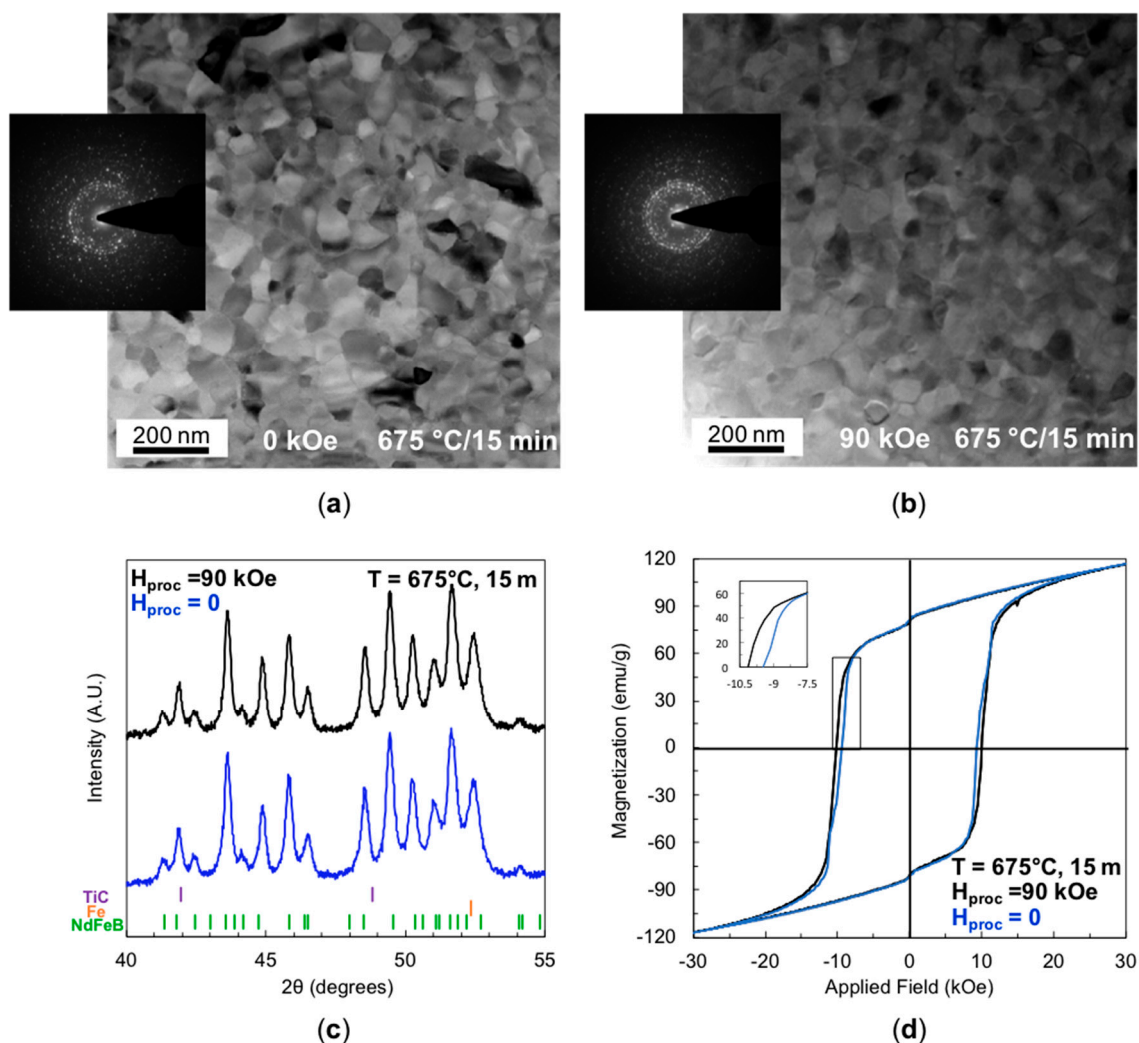
Figure 4. TEM bright field micrographs with SAD pattern insets from fully crystallized $Nd_2Fe_{14}B$ ribbons annealed at 675 °C for 15 min at (**a**) zero-field and (**b**) in an applied field of 90 kOe, along with the (**c**) XRD (Co Kα1 radiation, λ = 1.7890 Å) showing apparent identical spectra, and (**d**) VSM hysteresis curves of the fully crystallized ribbons at zero-field (blue) and in an applied field of 90 kOe (black) showing the magnetic behavior with an inset revealing a difference in coercivity.

3. Conclusions

Several examples of the effects of large magnetic fields during the microstructural evolution of strongly over-quenched, near-amorphous $Nd_2Fe_{14}B$ ribbons are presented. Several interesting experimental observations are made. (1) High magnetic fields have no detected effect on the crystallization peak associated with the $Nd_2Fe_{14}B$ phase determined by DSC. (2) When annealed for 30 min below the crystallization peak, intermediate fields promote the hard magnetic phase while higher fields suppress it. (3) Very short (thermally arrested) heat treatments below, near, and above the crystallization peak show suppression of the hard magnetic phase by a high field, and TEM observations suggest a much finer microstructure results in the high field. (4) Indications of grain size reduction and improved coercivity associated with a large processing field are seen when the microstructure is allowed to fully crystallize but not coarsen significantly well above the crystallization peak. While the origins of these behaviors are not well understood at this time, these results do highlight strong thermodynamic and kinetic effects of large fields during the processing of amorphous rare earth magnet materials and should motivate further detailed studies in the related mechanism and how they can be used to ultimately enhance magnetic performance.

4. Materials and Methods

4.1. Melt Spinning

Ingots of stoichiometric $Nd_2Fe_{14}B$ with the addition of 3 wt.% TiC alloy were prepared from high purity elements using a conventional arc melting method under ultra-high purity argon gas. Ingots were flipped and re-melted three times to ensure homogeneity. For the melt spinning process each ingot was placed into a quartz crucible fitted with a 0.81 mm precision capillary orifice. The charge was placed into a chamber filled with 1/3 atm. of ultra-high purity helium and induction heated to approximately 1375 °C as determined by a two-color infrared pyrometer. An overpressure of 120 Torr was used to eject the melt onto a rotating copper wheel with a tangential wheel speed of 25 m/s.

4.2. Heat Treatments

Ribbons were wrapped in Ta foil and encapsulated in quartz ampules under ultra-high purity argon at approximately 1/3 atmosphere. Heat treatments were conducted in an American Magnetics, Inc. superconducting magnet with a 5″ (12.7 cm) bore at zero-field and at applied fields of 20 kOe and 90 kOe. A PID controlled induction furnace with a steel susceptor was used for heating and temperature was monitored with two thermocouples, one for controlling and another for safety and consistency, that were in direct contact with the quartz ampule directly adjacent to the specimen. Samples were heated at a rate of 20 °C/min, held at temperature for either 3, 15, or 30 min, then pulled from the furnace and water quenched. K-type thermocouples were used in the annealing treatments and the temperature change for in-field experiments was evaluated. There was a 0.5 Kelvin/Telsa difference between K- and S-type thermocouples. Additionally, the induction furnace power output profile for an S-type thermocouple-controlled test was unchanged by field, while the K-type required a slight increase in power to maintain the setpoint, revealing that the K-type was reading a slightly lower temperature. The temperature difference was determined to be less than 4 Kelvin for in-field and zero-field experiments for the temperature range in this study.

4.3. Differential Scanning Calorimetry

A custom-built calorimeter [18] was used to evaluate the crystallization temperatures of the amorphous ribbons. The RF transparent quarts insert was placed inside a vertically aligned American Magnetics, Inc. superconducting magnet with a 5″ bore fitted with an induction coil. The DSC system was designed around a commercial SETARAM head that fit DSC and DTA sensors (S-type) with standard crucibles. The signal from the S-type sensor was shown to be unaffected by the applied magnetic field. A graphite susceptor inside the insert was used as the heat source. The heating was conducted at constant power with an average heating rate of 45 °C/min through the range of crystallization.

4.4. Magnetic Measurement

Data was obtained using a Quantum Design Versalab^{TM} vibrating sample magnetometer (VSM). The ribbon pieces were placed into a Quantum Design brass half-tube holder and secured into place with VGE-7031 varnish. A Quantum Design magnetic property measurement system (MPMS) was also used for magnetic measurements. For this technique, ribbons were glued to inside of a straw. For each device, a 30 kOe field was applied, at a temperature of 300 K, along the length of the ribbon pieces to minimize error from demagnetizing effects. No demagnetization correction factors were applied.

4.5. X-ray Diffraction

X-ray diffraction (XRD) was performed with a PANalytical X-Pert Pro diffractometer (Cu Kα1 radiation, λ = 1.5406 Å and Co Kα1 radiation, λ = 1.7890 Å). Multiple ribbons were tiled on the surface of a zero-background sample holder with the aid of a small quantity of silicone grease.

4.6. Transmission Electron Microscopy

Microstructural characterization was performed on a probe aberration corrected FEI Titan Themis scanning transmission electron microscope (TEM) with Super-X energy dispersive X-ray (EDS) detector and Lorentz lens. The TEM samples were prepared by mechanical wedge polishing followed by argon ion milling with liquid N_2 cold stage.

References

1. Sagawa, M.; Fujimura, S.; Togawa, N.; Yamamoto, H.; Matsuura, Y. New material for permanent magnets on a base of Nd and Fe (invited). *J. Appl. Phys.* **1984**, *55*, 2083–2087. [CrossRef]
2. Durst, K.-D.; Kronmüller, H. The coercive field of sintered and melt-spun NdFeB magnets. *J. Magn. Magn. Mater.* **1987**, *68*, 63–75. [CrossRef]
3. Brown, D.; Ma, B.-M.; Chen, Z. Developments in the processing and properties of NdFeb-type permanent magnets. *J. Magn. Magn. Mater.* **2002**, *248*, 432–440. [CrossRef]
4. Hono, K.; Sepehri-Amin, H. Strategy for high-coercivity Nd–Fe–B magnets. *Scr. Mater.* **2012**, *67*, 530–535. [CrossRef]
5. Liu, J.; Sepehri-Amin, H.; Ohkubo, T.; Hioki, K.; Hattori, A.; Schrefl, T.; Hono, K. Grain size dependence of coercivity of hot-deformed Nd–Fe–B anisotropic magnets. *Acta Mater.* **2015**, *82*, 336–343. [CrossRef]
6. Enokido, Y.; Miwa, M.; Goto, S.; Fujikawa, Y. Effects of Grain Boundary Phase on Coercivity of Dysprosium-Free Rare Earth Magnet. *Mater. Trans.* **2016**, *57*, 1960–1965. [CrossRef]
7. Choi, J.-K.; Ohtsuka, H.; Xu, Y.; Choo, W.-Y. Effects of a strong magnetic field on the phase stability of plain carbon steels. *Scr. Mater.* **2000**, *43*, 221–226. [CrossRef]
8. Joo, H.D.; Kim, S.U.; Koo, Y.M.; Shin, N.S.; Choi, J.K. An effect of a strong magnetic field on the phase transformation in plain carbon steels. *Metall. Mater. Trans. A* **2004**, *35*, 1663–1668. [CrossRef]
9. Onodera, R.; Kimura, S.; Watanabe, K.; Yokoyama, Y.; Makino, A.; Koyama, K. Isothermal Crystallization of Iron-Based Amorphous Alloys in a High Magnetic Field. *Mater. Trans.* **2013**, *54*, 1232–1235. [CrossRef]
10. Sun, Z.H.I.; Guo, M.; Vleugels, J.; Van der Biest, O.; Blanpain, B. Strong static magnetic field processing of metallic materials: A review. *Curr. Opin. Solid State Mater. Sci.* **2012**, *16*, 254–267. [CrossRef]
11. Rivoirard, S. High Steady Magnetic Field Processing of Functional Magnetic Materials. *JOM* **2013**, *65*, 901–909. [CrossRef]
12. Courtois, P.; Perrier de la Bâthie, R.; Tournier, R. Exploration of the magnetic field effect on the orientation of Nd2Fe14B crystallites at high temperatures. *J. Magn. Magn. Mater.* **1996**, *153*, 224–230. [CrossRef]
13. Kato, H.; Miyazaki, T.; Sagawa, M.; Koyama, K. Coercivity enhancements by high-magnetic-field annealing in sintered Nd–Fe–B magnets. *Appl. Phys. Lett.* **2004**, *84*, 4230–4232. [CrossRef]
14. Cui, B.Z.; Yu, C.T.; Han, K.; Liu, J.P.; Garmestani, H.; Pechan, M.J.; Schneider-Muntau, H.J. Magnetization reversal and nanostructure refinement in magnetically annealed Nd2Fe14B/α-Fe-type nanocomposites. *J. Appl. Phys.* **2005**, *97*, 10F308. [CrossRef]

15. Kato, H.; Koyama, K.; Takahashi, K. Crystallization of Nd-Co-B nanocomposite ribbons in high magnetic fields. *J. Appl. Phys.* **2011**, *109*, 07A726. [CrossRef]

16. McGuire, M.A.; Rios, O.; Conner, B.S.; Carter, W.G.; Huang, M.; Sun, K.; Palasyuk, O.; Jensen, B.; Zhou, L.; Dennis, K.; et al. Magnetic field control of microstructural development in melt-spun Pr2Co14B. *J. Magn. Magn. Mater.* **2017**, *430*, 85–88. [CrossRef]

17. Branagan, D.J.; McCallum, R.W. Solubility of Ti with C in the Nd2Fe14B system and controlled carbide precipitation. *J. Alloy. Compd.* **1995**, *218*, 143–148. [CrossRef]

18. Byvank, T.; Conner, B.; Kisner, R.; McGuire, M.; Rios, O.; Evans, B.; Nlebedim, C.; Kesler, M.; McCallum, R. High Command Fidelity Electromagnetically Driven Calorimeter. U.S. Patent US2018/0058953 A1, 1 March 2018.

19. Kramer, M.J.; Mecco, H.; Dennis, K.W.; Vargonova, E.; McCallum, R.W.; Napolitano, R.E. Rapid solidification and metallic glass formation—Experimental and theoretical limits. *J. Non-Cryst. Solids* **2007**, *353*, 3633–3639. [CrossRef]

20. Hubbard, J. Magnetism of iron. II. *Phys. Rev. B* **1979**, *20*, 4584–4595. [CrossRef]

21. Lichtenstein, A.I.; Katsnelson, M.I.; Kotliar, G. Finite-Temperature Magnetism of Transition Metals: An ab initio Dynamical Mean-Field Theory. *Phys. Rev. Lett.* **2001**, *87*, 067205. [CrossRef] [PubMed]